

Characterization of the Phase Contrast Imaging system based on the miniature synchrotron MIRRORCLE-6X

Joop van Heekeren,^{1, a)} Alexander Kostenko,^{1, a)} Takayasu Hanashima,² Hironari Yamada,² Sjoerd Stallinga,¹ S. Erik Offerman,³ and Lucas van Vliet¹

¹⁾*Quantitative Imaging Group, Department of Applied Sciences, Delft University of Technology, Lorentzweg 1, 2628 CJ Delft, Netherlands*

²⁾*Photon Production Laboratory Ltd, Ritsumeikan University, 1-1-1 Noji-higashi, Kusatsu, Shiga 525-8577, Japan*

³⁾*Department of Materials Science and Engineering, Delft University of Technology, Mekelweg 2, 2628 CD Delft, Netherlands*

This article provides a quantitative characterization of an *X-ray Phase Contrast Imaging (PCI)* system based on the miniature synchrotron technology MIRRORCLE-6X. The current implementation of the examined imaging system is a prototype of the so-called “in-line” modality of the *X-ray PCI*, which can, however, potentially be modified into prototypes of the other imaging modalities of the *X-ray PCI* family. Currently achievable levels of contrast due to the phase effect were measured using an edge response. Interpretation of the recorded performance is given using a comprehensive model based on the known characteristics of the system components. Monte-Carlo simulations are shown to be a useful tool in the analysis of the system spectral characteristics and resolution. The measured ratio of the detected phase contrast to the absorption contrast is currently in the range 100% to 200%. With the current design of the target mounting the minimum size of the target that can be efficiently used in MIRRORCLE-6X for an X-Ray imaging is of the order of $30 - 40 \mu\text{m}\phi$. Considering the measured data and the results of the modelling, a brief discussion is given to the potential development of the prototype, leading to the improvement of the phase contrast enhancement.

Keywords: Phase contrast imaging, miniature synchrotron, MIRRORCLE

I. INTRODUCTION

Phase Contrast Imaging (PCI) has first been introduced in optical microscopy¹ and later in transmission electron microscopy (TEM-PCI)² and X-ray imaging (X-PCI)³. Medical application of X-PCI would provide a number of possibilities for label-free soft-tissue imaging, e.g. for radiology of blood vessels (angiography), breast tissue (mammography), brain tissue (neuroimaging), cartilage etc⁴⁻⁶. There are a number of different methods to measure X-PCI⁷⁻¹⁰. *In-line* X-PCI is the most simple and straightforward method, as it requires only small modifications to the standard transmission imaging geometry. It does however, require a bench-top sized source with high coherence and brilliance. Competing methods are *gratings-based* X-PCI¹¹ and *aperture-based* X-PCI¹², which can operate with conventional X-ray sources, but require modifications to the imaging geometry.

The requirements on size and brilliance of the X-ray source that are posed by medical imaging to the *in-line* X-PCI have remained incompatible so far. Synchrotron facilities offer high brilliance but are too large-scale facilities and too expensive to comply with hospital infrastructures. Microfocus X-ray tubes, on the other hand, are small, but lack brilliance. The development of bench-top high-brilliance X-ray sources is thus of great importance for advancing the *in-line* X-PCI for medical application. Miniature synchrotron X-ray sources^{13,14} among other emerging technologies^{15,16} might provide the right combination of size and brilliance that is required for an effective implementation of the *in-line* X-PCI.

We have carried out a series of measurements using a prototype miniature synchrotron X-ray source MIRRORCLE-6X¹⁷.

The maximum contrast levels achievable with the current system in the X-PCI regime were compared to the contrast levels of the absorption image. Here we report on these measurements and on a model of the imaging process, including the X-ray source, the geometry and the detector. In particular, the design of the electron target appears to be crucial in obtaining high contrast levels, and several design improvements are deduced from the analysis we present here.

II. MATERIALS AND METHODS

A. MIRRORCLE-6X

The investigated imaging system is based on the compact synchrotron X-ray radiation source MIRRORCLE-6X. The synchrotron ring of the MIRRORCLE-6X contains an electron beam accelerated to the total energy of 6MeV. A small metallic target can be suspended on a Beryllium or Carbon filament inside the electron orbit to produce a white spectrum *Bremsstrahlung* radiation ranging from 0.001 to 6MeV¹⁸. A cone beam of the hard X-Rays leaves the synchrotron ring through a beryllium exit-window.

In the experiments presented in this paper the MIRRORCLE-6X was operated in the regime with an electron injection current 75mA and injection frequency 400Hz. Tungsten spherical targets of $10\mu\text{m}\phi$, $20\mu\text{m}\phi$ and $40\mu\text{m}\phi$ were used for X-ray generation. Each target was suspended inside an epoxy droplet attached to a $7.6\mu\text{m}\phi$ diameter carbon filament. The simulations and the analysis of the acquired data show that, a significant part of radiation is generated by the epoxy surrounding the target and the part of the target mounting that is exposed to the electron beam (roughly $\sim 1\text{mm}\phi$). This has a profound influence on the effective source size and its spectral characteristics and will

^{a)}Both first co-authors share an equal contribution to the current publication.

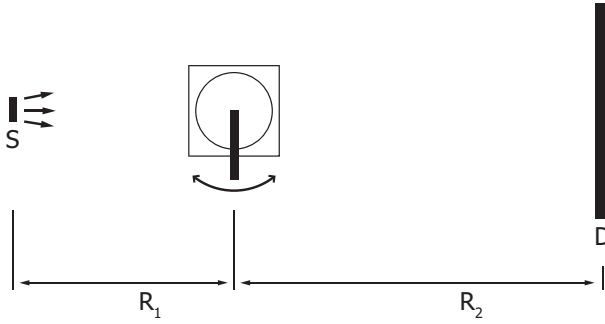


Figure 1: The sample is positioned between the X-ray source (S) and the detector (D) allowing for magnified imaging. Object-source distance is R_1 , object-detector distance is R_2 . The sample is mounted on a rotation stage in order to record phase images of the tilted edge.

be investigated in the Section III C.

B. X-ray detector

A $BaFBr : Eu^{2+}$ photo-stimulable phosphor imaging plate (IP) was used together with a FCR XL-1 image plate reader from Fujifilm (Tokyo, Japan) as X-ray detector. It is shown¹⁹ that the properties of the imaging plate are highly uniform over its surface, the response is linear relative to the radiation dose up to $4e4$ photons/ $100\mu m^2$ providing a wide dynamic range.

The estimations^{19,20} of the Full Width Half Maximum (FWHM) of the detector's point-spread function (PSF) are in the range of $170 \sim 200\mu m$. The quantum efficiency (QE) of the IP is given to be almost 100% at the energies below 20keV and dropping to about 50% at the energies above 35keV^{21,22}.

As the properties of the IPs vary between the different models, the PSF and its spectral characteristics were estimated by us independently. The PSF of the IP used in our experiment was estimated from the acquired reference beam-images using the noise method²³. The PSF was found to be approximately Gaussian shape with a FWHM of $260\mu m$. The images were sampled by the reader with a pixel pitch of $150\mu m$. Further discussion of the detector spectral characteristics is given in the Section III B.

C. Geometry of the setup

In the *in-line X-PCI* method the standard transmission imaging geometry with divergent beam is used (Figure 1). The specimen is mounted between the X-ray source and the detector with source-object distance R_1 and object-detector distance R_2 , providing magnification $M = (R_1 + R_2)/R_1$.

The phase image of the specimen has an interferometric nature and is observed as an intensity fringe located around the inhomogeneities of the projected refractive index of the object. Given certain propagation distances R_1 and R_2 the magnitude of the recorded phase image depends on the wavelength of the X-ray radiation and contrast transfer function (CTF) of the imaging system. Therefore the major factors that define the

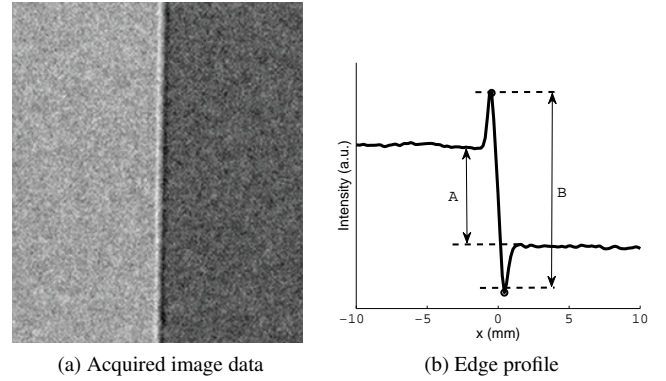


Figure 2: An image of a 1.95mm plexiglas plate is acquired in the X-PCI regime (a). An intensity fringe due to phase contrast is clearly visible on the image, slightly tilted relatively to the vertical axis. Image (b) shows a projected profile, calculated using the Radon transform of the image, accounting for a small tilt of the edge. The transmission contrast is indicated on the profile image as A, phase contrast enhancement is measured as the fringe amplitude $(B - A)/A$.

contrast of the *X-PCI* system of a given length are its spectral characteristics and the spatial resolution.

The experiments were carried out in high magnification regime with M in the range from 12 to 14.5 in order to reach the highest possible resolution in the object plane considering the PSF_{det} of the $BaFBr : Eu^{2+}$ detector. In such a regime the effective resolution of the imaging system is mainly limited by the source PSF_{src} .

D. Measurements

A thin plexiglas plate blocking part of the X-ray beam is often used as a standard specimen in the investigations of the performance of the *X-PCI* systems^{24,25}. The observed image in that case is a transmission image of the plate combined with the intensity fringe of the phase image that stretches along the plexiglas-air edge (Figure 2a). The image of such a specimen can be easily modeled, simplifying the analysis of the system performance.

The magnitude of the phase image fringe of the plexiglas plate is highly sensitive to the orientation of its edge to the direction of the beam, as the projection of the object changes. In our experiment the plexiglas plate (thickness 1.95mm) is mounted on a rotation stage so series of images can be recorded for a range of angles of incidence for every system setting (Figure 1).

E. Image processing and analysis

Since the plexiglas plate is homogeneous, it can be presented as a one-dimensional object simplifying the analysis. Several steps have to be taken before the raw measurements can be compared to the results of the model. First, a simple flat-field correction is done by dividing each acquired image by a reference beam-image. Next, using the Radon transform,

the image is integrated in the direction of the edge, resulting in one-dimensional edge profile (Figure 2b). The orientation of the edge can be found as an angle at which the Radon transform of the image yields the highest maximum derivative.

The ratio between the phase contrast and transmission contrast of the edge (Figure 2b) can be estimated for each image by measuring the fraction of the amplitude of the phase fringe $B - A$ to the intensity drop due to absorption of the plexiglas plate A . Ratio $(B - A)/A$ is used as an estimate of the sensitivity of the phase imaging system and is referred to in the text as a *phase contrast enhancement (PCE)*.

F. Calibration of the angle of incidence

The phase image and the transmission image of the plexiglas plate depend on the angle with which the radiation is incident on it. This results in a high sensitivity of the *phase contrast enhancement* to the angle of incidence. For that reason, each experiment consists of a series of images taken for a range of object orientations of approximately $\pm 3^\circ$. Using the fact that *PCE* must be symmetrical relative to the incidence angle 0° , the correction for a small misalignment in the object orientation could be done after the data acquisition.

III. MODEL

The MIRRORCLE-6X is a highly polychromatic X-ray source (spectrum $0.001 - 6\text{MeV}$) which requires an accurate account for polychromaticity during the analysis of the imaging process. The corresponding numerical model represents three main stages of the image formation: interaction of the polychromatic X-ray field with the object, propagation of the electromagnetic field to the X-ray detector and the model of the detection process based on the estimated spatial resolution and spectral characteristics of the X-ray detector and X-ray source.

A. Object interaction and field propagation

The description of the X-ray field interaction with the specimen is extremely straightforward in the current experiment. The plexiglas plate satisfies the condition of the thin-body approximation²⁶, therefore the field interaction is described by transmission function (1):

$$T(\mathbf{x}) = \exp(-\delta(x)) \cdot \exp(i\phi(\mathbf{x})), \quad (1)$$

where $\delta(x)$ is a linear attenuation map of the specimen and $\phi(\mathbf{x})$ is a phase map. The linear attenuation map $\delta(x)$ is calculated using the mass attenuation coefficients from the NIST database²⁷ and the known projected mass of the specimen. For the X-ray energies above the absorption edges of the material ($\gg 1\text{keV}$) the phase map can be very well approximated by²⁸:

$$\phi(\mathbf{x}) = -\lambda r_e N_e d(\mathbf{x}), \quad (2)$$

where λ is a wavelength of the electromagnetic field, r_e is the classical electron density, N_e is the electron density, $d(\mathbf{x})$ is a projected length.

The propagation of the monochromatic component of the electromagnetic field from the object plane to the detector plane is described by Fresnel diffraction. The computationally efficient Fourier formulation of Fresnel diffraction can be written as^{29,30}:

$$\psi_E(\mathbf{M}\mathbf{x}, R_2) = \frac{1}{M} \text{IFT} \left[\exp \left(\frac{i\lambda R_2 |\mathbf{u}|^2}{4\pi M} \right) \text{FT}[T(\mathbf{x})] \right], \quad (3)$$

where \mathbf{u} is the spatial frequency. In this equation the geometric magnification of the system M is accounted for and the phase pre-factor is dropped.

The total intensity of the field at the detector plane $I_d(\mathbf{x})$ will be calculated as a superposition of all propagated monochromatic components:

$$I_d(\mathbf{x}) = \int |\psi_E(\mathbf{x}, R_2)|^2 S(E) dE, \quad (4)$$

where $S(E)$ is the effective intensity spectrum of the system.

Due to a finite nature of the X-ray source, the detected image is formed as a superposition of intensity fields $I_d(x)$ produced by each point of the X-ray source independently. Considering that the source size is negligible relatively to the propagation length of the field, the result of the superposition is described as a convolution of the point-source intensity field $I_d(x)$ with the point-spread function $\text{PSF}_{\text{src}}(\mathbf{x})$ that corresponds to the source shape²⁶:

$$I(\mathbf{x}) = \text{PSF}_{\text{src}} \left(\frac{\mathbf{x}}{M-1} \right) * \text{PSF}_{\text{det}}(\mathbf{x}) * I_d(\mathbf{x}), \quad (5)$$

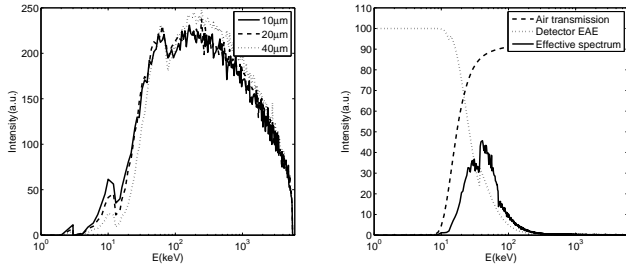
where $\text{PSF}_{\text{det}}(\mathbf{x})$ is a point-spread function of the X-ray detector. The factor $M - 1$ is introduced to account for demagnification of the projected source size.

Expression (5) completes the model described above, which allows to calculate an image of a known specimen detected in the *in-line X-PCI* system. The characteristics of the imaging system are included in the model as the effective spectrum $S(E)$, source and detector point-spread functions $\text{PSF}_{\text{src}}(\mathbf{x})$, $\text{PSF}_{\text{det}}(\mathbf{x})$. Accurate estimation of these functions is absolutely crucial for the modelling process and will be described in two following subsections.

B. System spectral characteristics. Detector efficiency.

The first step in modeling the imaging process is to estimate the effective spectrum of the system. The effective spectrum $S(E)$ is a product of the emission spectrum of the MIRRORCLE-6X $S_e(E)$, the energy dependent transmission of the system $T_s(E)$ and the energy absorption efficiency $EAE(E)$ of the detector:

$$S(E) = S_e(E) T_s(E) EAE(E). \quad (6)$$



(a) Normalized X-ray spectra of the spherical tungsten targets. (b) Effective spectrum of the imaging system based on the $40\mu\text{m}\phi$ tungsten target X-Ray source.

Figure 3: Spectra of $10\mu\text{m}\phi$, $20\mu\text{m}\phi$ and $40\mu\text{m}\phi$ tungsten spheres were computed using GEANT4 package. A monochromatic, spatially uniform electron beam with the total energy of 6MeV was assumed in the calculation. Estimation of the effective spectrum was done considering computed efficiency of the BaFBr:Eu detector and the transmission through the five meters of air.

The emission spectrum $S_e(E)$ of the MIRRORCLE-6X was calculated using Monte-Carlo simulations based on the GEANT4 toolbox³¹ (Figure 3). The energy dependent transmission of the system $T_s(E)$ is defined as the fraction of X-rays of a certain energy emitted by the source which reach the detector plane in the absence of an object. In the calculation of the system transmission $T_s(E)$, the absorption of X-rays by the beryllium exit-window of the MIRRORCLE and the air between the exit-window and the detector is accounted for.

The energy absorption efficiency $EAE(E)$ of the detector is defined as a fraction of X-ray intensity of a certain energy which is converted to a detector signal. It is given by³²:

$$EAE(E) = \left(\frac{\mu_{en}(E)}{\mu(E)} \right) \left(1 - e^{(-\mu(E)d)} \right), \quad (7)$$

here $\left(1 - e^{(-\mu(E)d)} \right)$ is the quantum detection efficiency (QDE), the fraction of X-ray photons which interact with the scintillator, with d the thickness of the active layer of the detector and $\mu(E)$ the mass attenuation coefficient of BaFBr. The mass energy-absorption coefficient divided by mass attenuation coefficient $\left(\frac{\mu_{en}(E)}{\mu(E)} \right)$ is the average fraction of energy transferred in each interaction with the active layer. Both coefficients $\mu_{en}(E)$ and $\mu(E)$ are well documented³³. The effective spectrum of the five meter long imaging system with $40\mu\text{m}\phi$ tungsten target and BaFBr:Eu detector is depicted on the figure 3b.

Calculation shows that the total intensity of the target is not linearly dependant on the volume, the photon fluxes of the $40\mu\text{m}\phi$ and $20\mu\text{m}\phi$ tungsten spheres were found to be correspondingly 26.2 and 4.5 times higher than that of $10\mu\text{m}\phi$. This can be explained by a self absorption in the target. The same phenomena contributes to a beam hardening, taking place in 20 – 40keV region, when the bigger target is used (Figure 3a). Such hardening of the emitted radiation lowers the sensitivity of the PCI system because the magnitude of the observed phase effect is proportional to λ^{-2} as it can be seen from (3)

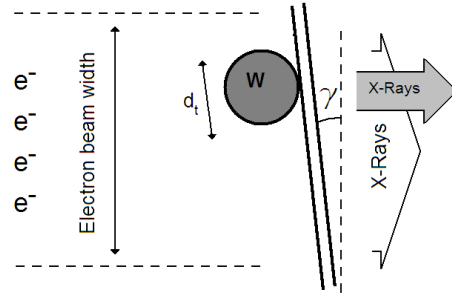


Figure 4: A schematic representation of the compound X-ray target.

and (4). On the other hand, high energy radiation might be more suitable because of the better transmission through the particular object of interest.

It is apparent, therefore, that the target size is an important characteristic of the X-Ray source, which influences the sensitivity of the system to the phase effect, defines the source point-spread function PSF_{src} , and the total brightness of the system. The configuration of the target can be optimized by using the Monte-Carlo simulations considering the characteristics of the complete imaging system in each particular case.

C. Compound target model: spectrum

The results of the Monte-Carlo simulations for the spectrum of the X-ray source, based on tungsten spherical targets (Figure 3a), correspond well with the measurements of the MIRRORCLE-6X brightness done in Yamada¹⁷. However, we have found that the so called 'compound target' model of the X-ray source may lead to a consistent interpretation of the phase contrast data that was obtained in our experiment.

It is known that in the MIRRORCLE-6X the tungsten target is suspended in a small droplet of epoxy attached to a thin carbon filament ($7.6\mu\text{m}\phi$). The whole construction is exposed to an electron beam of approximately $\sim 1\text{mm}\phi$ (Figure 4).

It was assumed that the interaction between the spherical tungsten targets, the epoxy droplet and the carbon filament is negligible during the X-Ray production. Spectra of the 'compound target model' were calculated as a superposition of independently simulated spectra of the source components. Calculations were done considering spherical $10\mu\text{m}\phi$, $20\mu\text{m}\phi$ and $40\mu\text{m}\phi$ tungsten targets, $70\mu\text{m}\phi$ sphere of epoxy and a carbon cylinder of $7.6\mu\text{m}\phi$ diameter exposed to an electron beam with Gaussian distribution with FWHM of 1mm.

Monte-Carlo simulation shows that an epoxy droplet and a carbon filament provide comparable or even larger contributions into the emission spectrum as the small tungsten target (Figure 5a, 5d, 5g). The fraction of the effective spectrum that is produced by the tungsten sphere is 33% for $10\mu\text{m}\phi$ target, 62% and 89% for $20\mu\text{m}\phi$ and $40\mu\text{m}\phi$ targets correspondingly. This has a profound influence on the behavior of the imaging system depending on the tungsten target size.

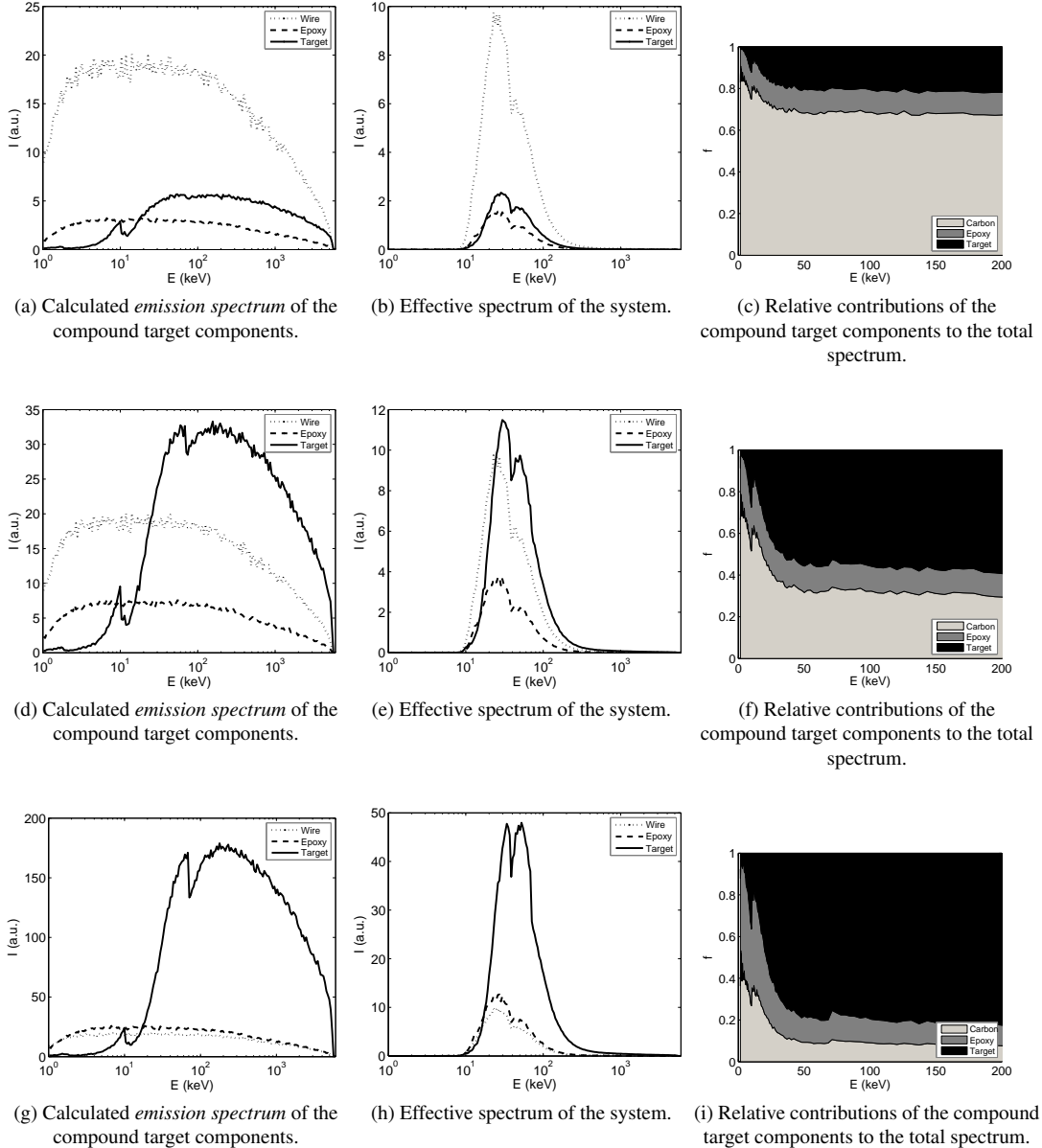


Figure 5: Normalized spectral characteristics (dose per solid angle unit) of the compound target components with $10\mu m\phi$ (top), $20\mu m\phi$ and $40\mu m\phi$ (bottom) tungsten sphere.

D. Compound target model: point-spread function

Compound target model provides an extremely anisotropic source point-spread function PSF_{src} determined by the projection of the emitting components of the source. In one of the two orthogonal dimensions of the image plane the PSF_{src} is determined by the projection of the tungsten target and epoxy droplet only, while in the other dimension the PSF_{src} has a much broader footprint due to the fraction of radiation produced by the carbon filament (FWHM $\sim 1mm$).

Unfortunately the data from the experiments with the plexiglas plate shows the performance of the imaging system in one dimension, which in each experiment has an a priori unknown orientation relative to the orientation of the suspending carbon filament. That forces us to introduce several fitting parameters

into the model in order to find a consistent interpretation of the measured data. To reduce the number of fitting parameters, it was decided to neglect the fraction of the PSF resulting from the epoxy droplet.

The first parameter is a fraction f of the X-rays that are not produced in the tungsten target but in the carbon filament. As a result, the image observed with the detector is the weighted sum of the image produced by the radiation from the target I_t and the filament I_w :

$$I = (1 - f)I_t + (f)I_w.$$

Images I_t and I_w will be distinct due to two principal phenomena. Firstly, the carbon filament and the target are emitting different X-rays spectra (Figure 5), therefore the phase effects

in images I_t and I_w are distinct. Secondly, the point-spread functions of the target $\text{PSF}_{\text{src},t}$ and the filament $\text{PSF}_{\text{src},w}$ are different due to the shape of the targets. If we assume that the X-ray production is homogeneous over the volume of the target and neglect absorption of X-rays inside the target, the shape of its $\text{PSF}_{\text{src},t}$ is equivalent to the projection of its volume. Because the image of the homogeneous plexiglas plate can be considered as a one dimensional edge profile, the point-spread function is projected onto a line perpendicular to the direction of the edge. We approximate the one-dimensional target $\text{PSF}_{\text{src},t}$ as a normalized projection of a sphere with radius R :

$$\text{PSF}_{\text{src},t}(x) = \begin{cases} \frac{3}{4R^3} (R^2 - x^2) & x < R \\ 0 & x \geq R \end{cases}. \quad (8)$$

The projected PSF of a cylindrical filament with radius R is likewise:

$$\text{PSF}_{\text{cylinder}}(x) = \begin{cases} \frac{2}{\pi R^2} \sqrt{R^2 - x^2} & x < R \\ 0 & x \geq R \end{cases}. \quad (9)$$

Generally, there is a small angle γ between the direction of the filament and the edge of the plexiglas plate (figure 4). This extends the $\text{PSF}_{\text{src},w}$ by the projection of the profile of the *electron beam* along the filament onto a line perpendicular to the edge. If we assume that the *electron beam* has a Gaussian-shaped intensity distribution along the filament with a FWHM of h , the projection of the beam PSF_{beam} is also Gaussian-shaped with a FWHM of $h \sin \gamma$. Therefore, the full $\text{PSF}_{\text{src},w}$ of the filament is:

$$\text{PSF}_{\text{src},w}(x) = \text{PSF}_{\text{cylinder}}(x) * \text{PSF}_{\text{beam}}(x, h \sin \gamma). \quad (10)$$

The mounting of the target on the side of the filament (Figure 4) causes a potential misalignment of the centers of the filament and the sphere. This causes an arbitrary spatial shift Δx between the intensity images I_t and I_w .

The observed phase-contrast edge profile $I(x)$, taking all described effects into account, is given by:

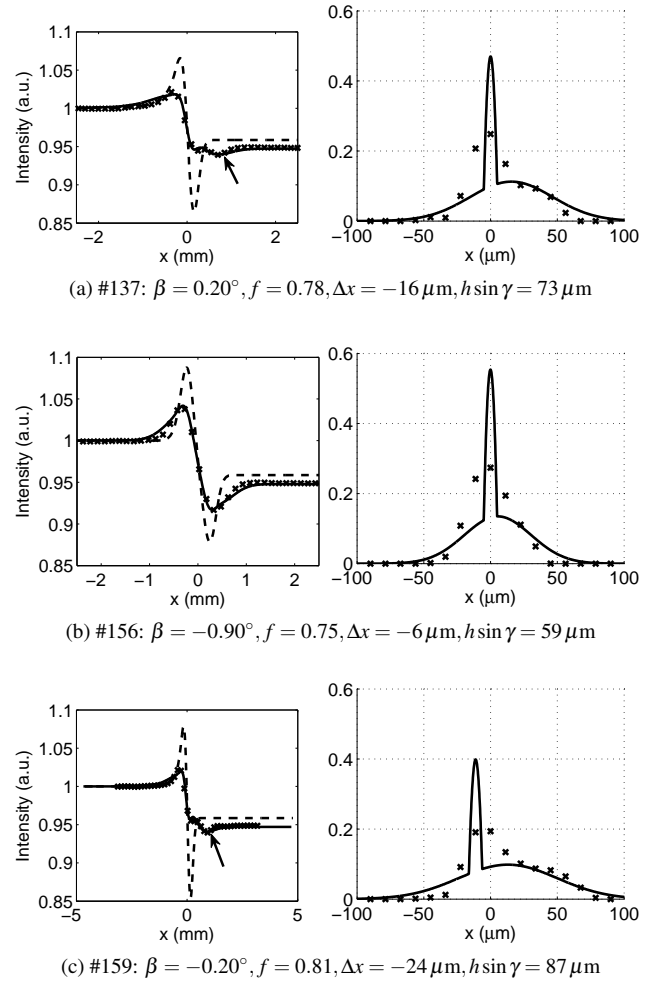


Figure 6: On the left: three profiles (crosses) measured at different angles of incidence β with magnification $M = 14.3$, system length $R_1 + R_2 = 5.41$ m, a $10 \mu\text{m}$ tungsten spherical target. Note the extra wiggle depicted with a small arrow in (a) and (c). The dashed lines are the modeled results for an ideal spherical target ($f = 0$) and the solid lines are the results for the compound target model with the indicated parameters. Right: the PSF_{src} estimated with a Wiener filter (crosses). The solid lines are the calculated PSFs for the fitted parameters (eq. (10)).

$$I(x) = (1-f) \text{PSF}_{\text{src},t} \left(\frac{x}{M-1} \right) * \text{PSF}_{\text{det}}(x) * I_t(x + [M-1]\Delta x) + (f) \text{PSF}_{\text{src},w} \left(\frac{x}{M-1}, h \sin \gamma \right) * \text{PSF}_{\text{det}}(x) * I_w(x) \quad (11)$$

IV. RESULTS

In the current paper we present the results of four series of 43 measurements of the phase contrast enhancement of the 1.95mm thick plexiglas plate.

As described in the Section II C each series of images is taken for a range of edge orientations ($\sim \pm 3^\circ$) relatively to the direction of the X-ray beam. Some examples of the acquired

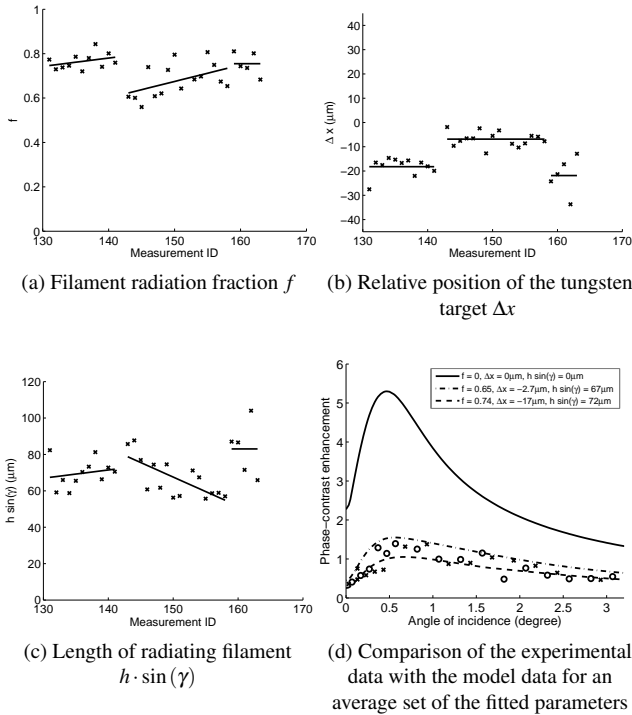


Figure 7: **(a, b, c)** The result from fitting the source parameters for a series of measurements. The solid lines indicate trends in the data over time. **(d)** The measured (crosses and circles) and modeled (lines) phase-contrast enhancement. The crosses indicate measurements done at negative angles of incidence. The solid line is the result for $f = 0$ and the dashed lines are the results for two typical sets of values from (a), (b) and (c). Measurements done with $M = 14.3$, $R_1 + R_2 = 5.41$ m, a $10\mu\text{m}$ tungsten spherical target

profiles are shown on the figures 6a,6b,6c. Figures demonstrate a large discrepancy between the measured edge profiles and the results of calculation based on the spherical target model.

Introduction of the *compound target* model, described in Section III C, allows for a very accurate reproduction of the measured data, however requires fitting of the parameters f , $h \cdot \sin(\gamma)$, Δx that represent misalignment between the orientation of the plexiglas edge and the components of the X-ray source.

The source point-spread function PSF_{src} was estimated using Wiener deconvolution of the acquired images with the profile resulting from the model based on the fitted parameters. It is shown on the figures 6a,6b and 6c that the estimated PSF_{src} corresponds with the PSF_{src} of the compound target model.

A. Stability of fitting

Results of fitting the model parameters for an experimental session are presented on figures 7a, 7b and 7c. The session consists of 31 measurement taken in the orientations range $\pm 3^\circ$, with magnification $M = 14.3$, system length $R_1 + R_2 =$

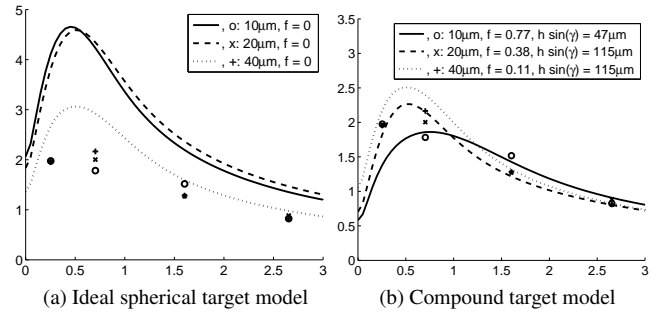


Figure 8: The phase-contrast enhancement for three series measured with tungsten spherical targets with diameters of 10, 20 and $40\mu\text{m}$ (correspondingly circles, crosses, plus-signs). Measurements were done with the same setup geometry $M = 12.8$ and $R_1 + R_2 = 5.31$ m. (a) demonstrates the discrepancy between the measured data and calculated values (solid, dash, point-line) using the ideal spherical target and (b) shows the result calculated with *compound target model*.

5.41m, using a $10\mu\text{m}$ tungsten target.

A considerable variation of the parameters throughout the series is apparent, however, linear trends in their variation can be found when the experimental session is divided into three groups of measurements (#131-141, 143-157 and 158-162) (Figures 7a, 7b and 7c). This may be explained with two re-sets of the setup that took place exactly after the measurement #141 and #157 was taken. A linear change in the parameters, that are describing the compound target, may be explained by a micro drift of the X-Ray source orientation during the measurement.

Such drift will of course not be relevant if the target PSF_{src} is isotropic, which can potentially be achieved by reduction of the carbon filament fraction that is exposed to the electron beam in MIRRORCLE-6X or increasing the volume of the spherical part of the target.

Figure 7,d demonstrates that a reasonable match between the experimental values of the *phase contrast enhancement* and the modeled values can be achieved using only the average values of the fitted parameters. The compound target model shows that the *phase contrast enhancement PCE* of the current system is decreased in the performed experiment with a factor of 2 to 5 compared to the system with the same geometry but using an ideal $10\mu\text{m}$ spherical tungsten target.

Another illustration of the results obtained with the compound target model is given in figure 8. The experimental series are acquired with magnification $M = 12.8$, system length $R_1 + R_2 = 5.31$ m, using $10\mu\text{m}$, $20\mu\text{m}$ and $40\mu\text{m}$ tungsten target. The *compound target* model uses values for f obtained in Monte-Carlo simulations of the X-ray emission by the target components (Section III C) and the other two parameters (Δx , $h \sin \gamma$) are found by least-square fitting.

The *PCE* predicted using the model with an ideal spherical target is too large for the small targets by approximately a factor of 2 in the current case (Figure 8a). The results of the *compound target* model, on the other hand, are very close to the experimental data. They do not only reproduce a gener-

ally lower *PCE* in all three experiments but also the trend that the contrast may be higher in some cases in the system with a larger target.

Namely, the $40\mu\text{m}\phi$ tungsten target dominates the rest of the emitting components of the MIRRORCLE-6X (providing 89% of radiation according to the Monte-Carlo simulations) and that is why it can yield a better performance than the smaller targets due to effectively sharper point-spread function. This also explains why the experiment that involves the bigger target is less influenced by the anisotropy of the MIRRORCLE-6X source (Figure III C, a).

B. Phase contrast enhancement of MIRRORCLE-6X

The levels of the contrast increase of the sharp plexiglas edge due to the *phase effect* of the MIRRORCLE-6X were observed to be between 100% and 200% in the current implementation. However, an accurate measurement of *PCE* was found to be particularly unstable. The instability can be explained by a high anisotropy in the resolution of the system caused by the radiation emitted from the components of the X-Ray source.

According to calculation, if no (or almost no) radiation is produced by the components other than the target, the current system based on MIRRORCLE-6X will yield a *PCE* of 400% to 500% (Figure 7d). That could be potentially achieved using constructions made of carbon nanomaterials. Effective reduction of the X-Ray source size below $30 - 40\mu\text{m}\phi$ can be in principle achieved without any modifications in the MIRRORCLE-6X design. A system of double bend Laue monochromators³⁴ would be required for patient imaging to select the appropriate x-ray spectrum and to limit the source size. A choice of X-Ray detector with higher resolution ($\lesssim 50\mu\text{m}$) will allow to use the geometry with lower magnification which yields even higher levels of the *PCE*.

According to Yamada³⁵, the micro-target of the MIRRORCLE-6X must be capable to produce a total X-Ray flux of an order of about $10^9\gamma/(s \cdot \text{mrad}^2 \cdot 0.1\% \text{band})$, which means that monochromatized beams with fluxes ranging from $10^7\gamma/(s \cdot \text{mrad}^2)$ to $10^9\gamma/(s \cdot \text{mrad}^2)$ should be available, depending on the bandwidth of the monochromator.

Another promising solution is to implement an imaging modality that requires arrayed X-Ray source. For example a *grating X-PCI* system can be designed, using an array of wires or a grating mounted in the electron beam of the synchrotron. A transition to a digital detector and addition of the monochromator is of course inevitable in the gratings-based system.

V. CONCLUSIONS

Performance of the *X-PCI* prototype based on MIRRORCLE-6X X-Ray source was characterized by us using the edge response of the system. *Phase contrast enhancement* factor was measured in series of experiments as a ratio between the phase and absorption contrast produced by the plexiglas plate. It was found to be particularly sensitive to the edge orientation due to a high anisotropy of the X-Ray source point-spread function. The observed *PCE* values

were found to be between 100% and 200% in different measurements.

The role of the X-Ray source target size was investigated using Monte-Carlo simulations package GEANT4. Calculations show that the target size has a considerable influence on the low-energy part of the emission spectrum ($10 - 40\text{keV}$, of a total $0.001 \sim 5.5\text{MeV}$). And what is more important, the components of the mounting of the target may emit up to 70% of the total radiation in case of $10\mu\text{m}\phi$ spherical tungsten target, down to 10% for the $40\mu\text{m}\phi$ targets.

As a result, the same or higher performance in terms of *PCE* values was observed in experiments when $40\mu\text{m}\phi$ target was used instead of $10\mu\text{m}\phi$ and $20\mu\text{m}\phi$ targets. The emission produced by the components of the mounting can not be fully avoided in the current implementation of the system due to the limited focusing of the electron beam in the synchrotron ring. This most likely limits the minimal diameter of the tungsten target that can be effectively used to $30 - 40\mu\text{m}\phi$ unless a thinner target mounting can be implemented. Calculations demonstrate that by significant reduction of the radiation emitted by the target mounting, the *PCE* levels of the MIRRORCLE-6X can be improved by a factor of 2 to 5 by allowing to use smaller targets.

REFERENCES

- ¹F. Zernike, "Phase-contrast, a new method for microscopic observation of transparent objects," *Physica*: 9, 686–698, 974–986 (1942).
- ²W. Coene, G. Janssen, M. O. de Beeck, and D. V. Dyck, "Phase retrieval through focus variation for ultra-resolution in field-emission transmission electron microscopy," *Physical Review Letters* **69**, 3743–3746 (1992).
- ³A. Snigirev, I. Snigireva, V. Kohn, S. Kuznetsov, and I. Schelokov, "On the possibilities of X-ray phase contrast microimaging by coherent highenergy synchrotron radiation," *Review Scientific Instruments* **66**, 5486 (1995).
- ⁴R. A. Lewis, "Medical phase contrast X-ray imaging: current status and future prospects," *Physical in Medicine and Biology* **49**, 3573–3583 (2004).
- ⁵J. Li, Z. Zhong, D. Connor, J. Mollenhauer, and C. Muehleman, "Phase-sensitive x-ray imaging of synovial joints," *Osteoarthritis and Cartilage* **17**, 1193–1196 (2009).
- ⁶A. Momose, T. Takeda, and Y. Itai, "Blood vessels: Depiction at phase-contrast x-ray imaging without contrast agents in the mouse and rat—feasibility study," *Radiology* **217**, 593 (2000).
- ⁷P. Cloetens, R. Barrett, J. Baruchel, J.-P. Guigay, and M. Schlenker, "Phase objects in synchrotron radiation hard x-ray imaging," *Journal of Physics D: Applied Physics* **29**, 133–146 (1996).
- ⁸D. Chapman, W. Thomlinson, R. E. Johnston, D. Washburn, E. Pisano, N. Gmür, Z. Zhong, R. Menk, F. Arfelli, and D. Sayers, "Diffraction enhanced X-ray imaging," *Physics in Medicine and Biology* **42**, 2015–2025 (1997).
- ⁹A. Momose, T. Takeda, Y. Itai, A. Yoneyama, and K. Hirano, "Phase-contrast tomographic imaging using an x-ray interferometer," *Journal of Synchrotron Radiation* **5**, 309–314 (1998).
- ¹⁰T. Weitkamp, A. Diaz, and C. David, "X-ray phase imaging with a grating interferometer," *Optics Express* **13**, 6296–6304 (2005).
- ¹¹F. Pfeiffer, T. Weitkamp, O. Bunk, and C. David, "Phase retrieval and differential phase-contrast imaging with low-brilliance x-ray sources," *Nature Physics* **2**, 258 (2006).
- ¹²A. Olivo and R. Speller, "A coded-aperture technique allowing X-ray phase contrast imaging with conventional sources," *Applied Physics Letters* **91** (2007), 10.1063/1.2772193.
- ¹³D. Hasegawa, H. Yamada, A. Kleev, N. Toyosugi, T. Hayashi, I. T. Yamada, and Y. Ro, "The tabletop synchrotron mirrorcle-6x," in *Proc. 14th Sympo. Accelerator Science and Technology and Tsukuba* (2003).
- ¹⁴M. Bech, O. Bunk, C. David, R. Ruth, R. L. Jeff Rifkin, R. Feidenhansl, and F. Pfeiffer, "Hard x-ray phase-contrast imaging with the compact light

- source based on inverse Compton x-rays," *Journal of Synchrotron Radiation* **16**, 43–47 (2008).
- ¹⁵T. Tuohimaa, M. Otendal, and H. M. Hertz, "Phase-contrast X-ray imaging with a liquid-metal-jet-anode microfocus source," *Applied Physics Letters* **91** (2007).
- ¹⁶R. Kincaid and et al., "Development of ultrafast laser-based X-ray in-vivo phase-contrast micro-CT beamline for biomedical applications at advanced laser light source (alls)," *Proc Soc Photo Opt Instrum Eng* **7078**, 707818.1–707818.12 (2008).
- ¹⁷H. Yamada, "Novel x-ray source based on a tabletop synchrotron and its unique features," *Nuclear Instruments and Methods in Physics Research B* **199**, 509–516 (2003).
- ¹⁸H. Toru, Y. Hironari, S. Makoto, HasegawaDaisuke, M. Masaki, O. Yasuhito, T. Jyunya, H. Takayasu, N. Norihisa, and T. Masashi, "Refraction contrast 11×-magnified x-ray imaging of large objects by mirrorcylinder-type table-top synchrotron," *Journal of Synchrotron Radiation* **13**, 397–402 (2006).
- ¹⁹U. Shmueli and A. J. C. Wilson, "International tables for crystallography," *Springer* **3**, 637–639 (2004).
- ²⁰M. Thoms, S. Bauchau, D. Hausermann, M. Kunz, T. L. Bihan, and M. Mezouar, "An improved x-ray detector for use at synchrotrons," *Nuclear Instruments and Methods in Physics Research A* **413**, 175–184 (1998).
- ²¹P. Witt, "Detective quantum efficiency of storage phosphors for soft X-rays," *Pure Applied Optics* **2**, 61–70 (1993).
- ²²M. Thoms, "The quantum efficiency of with image radiographic imaging plates," *Nuclear Instruments and Methods in Physics Research A* **378**, 598–611 (1996).
- ²³J. C. Dainty and R. Shaw, "Image science: principles, analysis and evaluation of photographic-type imaging processes," London: Academic Press (1974).
- ²⁴E. F. Donnelly, K. G. Lewis, K. M. Wolske, D. R. Pickens, and R. R. Price, "Characterization of the phase-contrast radiography edge-enhancement effect in a cabinet X-ray system," *Physical in Medicine and Biology* **51**, 21–30 (2006).
- ²⁵X. Z. Wu and H. Liu, "Clarification of aspects in in-line phase-sensitive X-ray imaging," *Medical Physics* **34**, 737–743 (2007), 139HZ Times Cited:4 Cited References Count:34.
- ²⁶X. Wu and H. Liu, "An experimental method of determining relative phase-contrast factor for x-ray imaging systems," *Medical Physics* **31**, 997–1002 (2004).
- ²⁷M. Berger, J. Hubbell, S. Seltzer, J. Chang, J. Coursey, R. Sukumar, and D. Zucker, "Xcom: Photon cross sections database," *NIST Standard Reference Database* **8**, 87–3597 (1998).
- ²⁸S. W. Wilkins, T. E. Gureyev, D. Gao, A. Pogany, and A. W. Stevenson, "Phase-contrast imaging using polychromatic hard X-rays," *Nature (London)* **384**, 335–338 (1996).
- ²⁹J. Goodman, *Introduction to Fourier optics* (Roberts & Company Publishers, 2005).
- ³⁰D. Paganin, *Coherent X-Ray Optics* (Oxford University Press, USA, 2006).
- ³¹Agostinelli, S., Allison, J., Amako, K., Apostolakis, J., Araujo, H., Arce, P., Asai, M., Axen, D., S. Banerjee, Barrand, G., et al., "Geant4: a simulation toolkit," *Nuclear Inst. and Methods in Physics Research and A* **506**, 250–303 (2003).
- ³²J. Beutel, H. L. Kundel, R. L. V. Metter, M. Sonka, M. Fitzpatrick, Y. Kim, and S. C. Horii, *Handbook of Medical Imaging: Display and PACS*, Handbook of Medical Imaging, Vol. 3 (SPIE Press, 2000).
- ³³J. H. Hubbell and S. M. Seltzer, *NISTIR 5632, Tables of X-ray mass attenuation coefficients and mass energy-absorption coefficients*, Tech. Rep. (National Institute of Standards and Technology).
- ³⁴Y. I. Nesterets and S. W. Wilkins, "A flexible configuration for a high-energy phase-contrast imaging beamline involving in-line focusing crystal optics," *Radiation Physics and Chemistry* **75**, 1981–1985 (2006).
- ³⁵H. Yamada, T. Hirai, M. Morita, T. Hanashima, M. Sasaki, D. Hasegawa, T. Hayashi, T. Yamada, , and H. Saisho, "Portable synchrotron hard x-ray source mirrorcylinder-6x for x-ray imaging," *Proc. 8th Int. Conf. X-ray Microscopy, IPAP Conf. Series 7* , 130–132 (2005).